CHAPTER FOUR

THE RELATIVISTIC TWIN PRECESSING BEAMS MODEL

4.0 To explain the inversion symmetry observed in many radio sources (e.g., Cyg A in Fig. 1.1 (see also Perley, Dreher & Cowan 1984), B2 0055+26 (Ekers et al. 1978), 0816+526 (Burns & Christiansen 1980)), the beam model can be modified to allow precession of the central engine which produces two oppositely directed continuous streams of plasma. It is found that many asymmetric sources with interesting structures like sharp bends can also be modelled by emission from twin precessing relativistic beams, projected on the plane of the sky (Gower et al. 1982). Hjellming & Johnston (1981) have given a detailed treatment of the kinematics of the model.

4.1 THE MODEL Relativistic plasma is continuously ejected at a speed $v = \beta c$ by the central engine whose ejection axis precesses conically with half-angle ψ and period P, the axis of the cone being inclined at angle i to the line of sight. For high speeds β and small inclination angles i, the structure is asymmetric both in intensity contrast and relative distance along the two branches of the bifurcated source, the receding beam being fainter and smaller than the approaching one. To get a roughly symmetric morphology, small β and large i are required.

Looking at various examples of inversion symmetric sources, we see that there are two kinds: one with some sort of 'continuity'

from one hotspot to the central radio core (or optical galaxy or quasar) to the other hotspot (e.g., Cyg A (Fig. 1.1 and Perley, Dreher & Cowan 1984; also compare with Fig. 8 of Simkin 1979, who has given the rotation axis of the parent galaxy superposed on Hargrave & Ryle's (1974) map which we have reproduced in Fig. 1.1) and 0816+526 (Burns & Christiansen 1980)) and another in which diffuse emission, beginning at the two hotspots, trails away from the line(s) pointing from these hotspots to the core (or optical object) (e.g., B2 0055+26 (Ekers et al. 1978)). We call the first kind S shaped sources (including the inverted shape Ƨ) and the second kind Z shaped sources (including the inverted shape Ƨ). In the precessing beams model, these are sources with large inclinations i to the line of sight, with precession significantly slower than advance of the beam giving rise to S shape and precession much faster than advance producing Z shape. Thus, in this scheme, a given source starts off with an S shape and after $\gtrsim 1\frac{1}{2}$ cycles of the precession, can attain a Z shape if the radiating material in the inner parts has by then faded out.

We now describe the model in more detail and write down the essential equations, and present results of applying it to the source 1857+566 in section 4.2 below. Choosing the origin of coordinates at the central engine and the x-axis pointing toward us (i.e., the observer), the yz-plane coincides

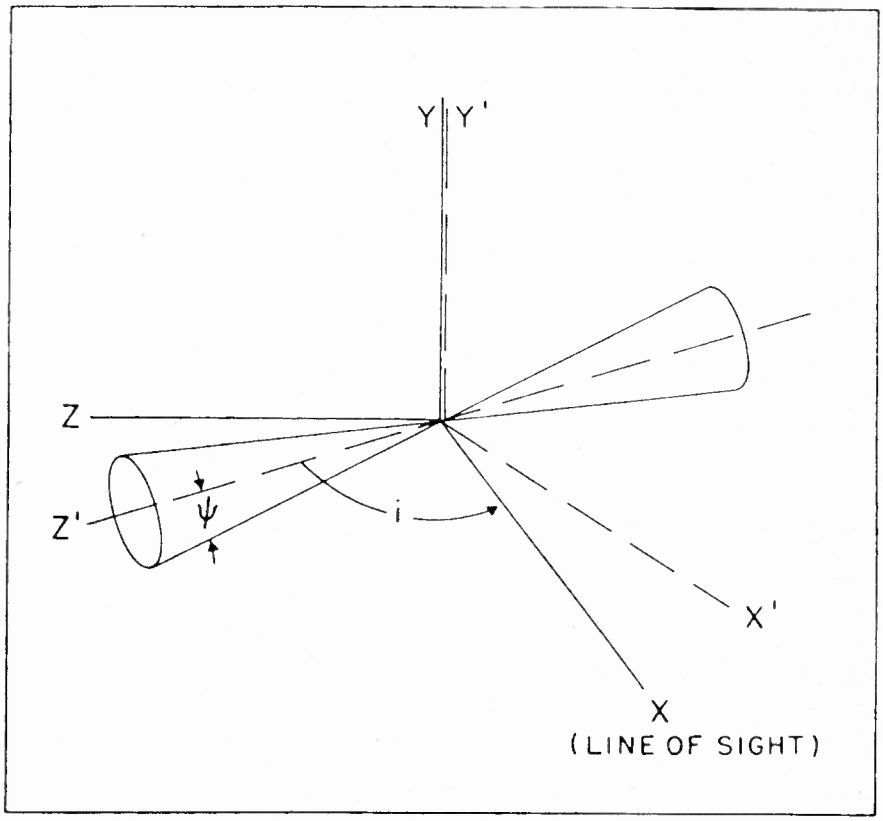

Fig. 4.1 Geometry of the relativistic precessing beams model

with the sky-plane (Fig. 4.1). Denote by Φ the azimuthal angle of an element of fluid of the relativistic plasma coming toward us in the stream which forms the beam. The velocity of this element can be resolved into three components in the standard way:

$$v_x = S_{beam} \beta c \{\sin \psi \sin i \cos \Phi + \cos \psi \cos i\} ,$$

$$v_y = S_{beam} \beta c \sin \psi \sin \Phi ,$$

$$v_z = S_{beam} \beta c \{\cos \psi \sin i - \sin \psi \cos i \cos \Phi\} ,$$

where $S_{beam} = +1$ for an element in the approaching beam and $S_{beam} = -1$ for the corresponding element in the receding beam. To get the position of an element on the sky-plane at the time of observation, v_y and v_z must be multiplied by the time interval Δt_{obs} (in the observer's frame of reference) since ejection of this element of fluid. Account must be taken of the light-travel-time from the position of the element to the observer in this calculation. This time interval is proportional to the increment in the azimuthal angle since ejection. All possible azimuthal angles since ejection give the trajectory of the beam on the sky-plane. If ϕ_o is the azimuth of the fluid element ejected at the time of observation, the azimuths of all the elements ejected earlier are given by

$$\phi = \phi_o - (\phi_I - \phi) = \phi_o - \frac{2\pi}{P} \Delta t_{obs} ,$$

on varying ϕ from ϕ_I to 0 (Δt_{obs} from 0 to a maximum). If the

distance of the source from us is D, the dimensionless angular coordinates Q_z and Q_y of an arbitrary point on the beam trajectory are:

$$Q_{z,y} \equiv \theta_{z,y} / (Pc/2\pi D) = (v_{z,y}/c)(\phi_I - \phi)/(1-v_x/c).$$

$\theta_{z,y}$ are the angular coordinates in radians, and $Q_{z,y}$ in units of $Pc/2\pi D$ (where P is the precession period). The shape of the trajectory can thus be obtained by plotting $Q_{z,y}$ with arbitrary scale. The parameters which completely specify the shape and extent of the trajectory are thus: β, ψ, i, ϕ_I and ϕ_o. To get the precession period in yrs (P_{yr}), we must match some feature of size θ_{arcsec} (e.g., the distance between the core and a hotspot, or that between two knots in a jet) in the observed (radio) map with the corresponding feature of size Q in the model trajectory:

$$P_{yr} = 90\ \theta_{arcsec}\ D_{Mpc} / Q.$$

In the model calculation, we have adjusted the trajectory to the maximum space available for plotting and noted the side of this square in terms of Q.

To calculate the image intensity, we must model the spreading and dimming of the radiating fluid elements as they age. The intensity at each grid-point in the plot is the sum of contributions at that point due to radiation from all points of the beam. We assume a Gaussian spreading, with width

increasing as the square-root of the proper age (model A of Scheuer 1974)

$$\Delta t_{obs} \; / \; (1-v^2/c^2)^{\frac{1}{2}} \; \propto \; (\phi_I - \phi) / (1-v^2/c^2)^{\frac{1}{2}},$$

and dimming proportional to the proper age. If there are N fluid elements in the approaching branch of the trajectory and N in the receding one, the intensity at a point (y,z) in the image is

$$I(y,z) \; \propto \; \sum_{i=-N}^{N} f_i(r_i) / (\phi_I - \phi_i) \left[(1-v_{xi}/c) / (1-v_i^2/c^2)^{\frac{1}{2}} \right]^{2+\alpha},$$

$f_i(r)$ specifies the spread,

where α is the spectral index, taken to be 1, and

$r_i^2 = (y-Q_{yi})^2 + (z-Q_{zi})^2$ is the distance of (y,z) from the centre of the ith fluid element (Q_{yi}, Q_{zi}). The factor with v_{xi} and v_i takes care of the different light-travel-times and Doppler boosting/dimming for different points of the beam. The proportionality constant is chosen to give the image an appropriate dynamic range, the limit being set by the maximum integer representable by the computer, 32767. I(y,z) is calculated at 100 points in a 10x10 matrix. The plot can be obtained either in a gray scale (with the number of dots in a single picture element quantifying the scale) or as a contour plot. Since the observed spread is the actual spread convolved with the telescope beam, and since two Gaussians convolved with each other give another Gaussian, we assume a Gaussian form for the observed spread:

$$f_i(r) = f_{0i} \exp[-r^2/r_{0i}^2],$$

$$r_{0i} = r_0 (\phi_I - \phi_i)^{\frac{1}{2}}.$$

With proper normalization, f_{0i} and r_0 are related by

$$\int_0^\infty 2\pi r \, dr \, f_i(r) = 1 \leftrightarrow f_{0i} = 1/\pi r_o^2 (\phi_I - \phi_i).$$

The spectral index α, the power-law index (= -1) for dimming of the radiating fluid elements and the power-law index (=½) for spreading of the elements are the new parameters needed for modelling the intensity, in addition to those listed earlier for the trajectory.

Gower et al (1982) have applied this model to a wide variety of structures, also varying the rate of precession for some cases. The fits seem to be better for the more asymmetric sources, for which high values of β are needed. We attempted to model some symmetric sources observed with the VLA (Alok Patnaik, private communication) and conclude that a deceleration of the beam against the intergalactic medium must be included in the model to account for the hotspots at the outer ends of the symmetric sources. Without such a provision, the only way to get an enhancement of intensity is to view a large amount of material coming toward us along the line of sight.

4.2 APPLICATION TO THE HIGH-REDSHIFT QUASAR 1857+566 In this section we present results of applying the model of section 4.1

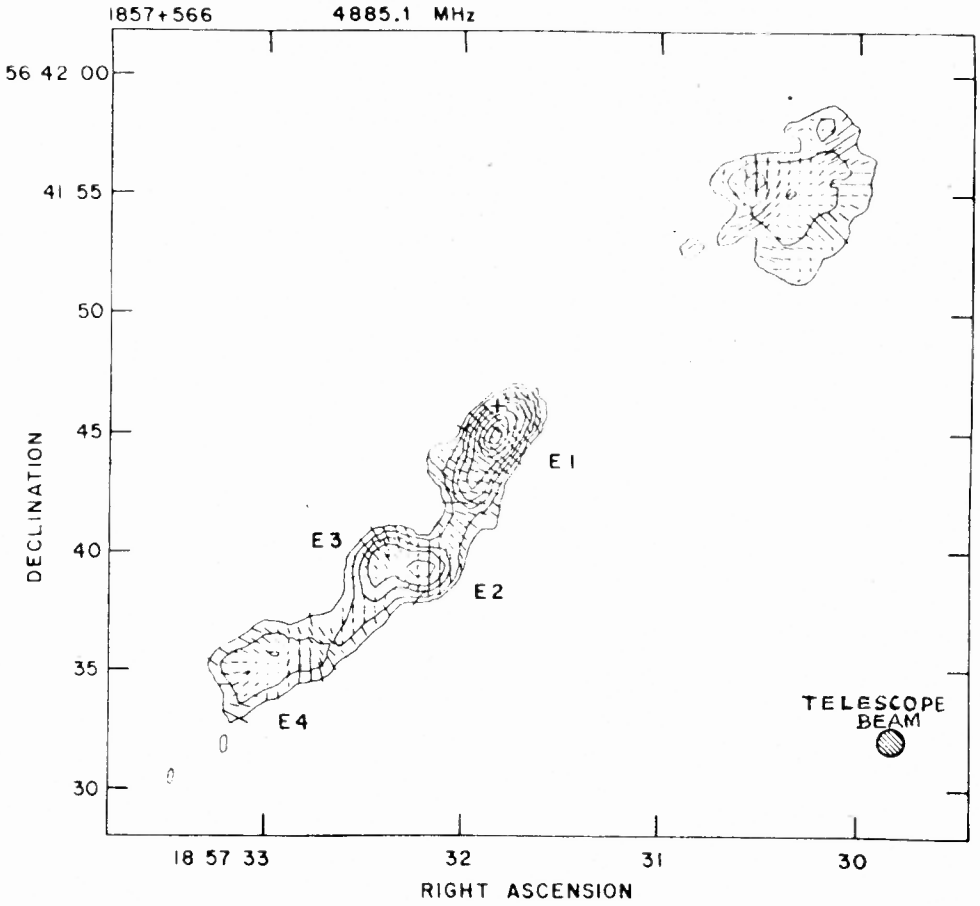

(a)

Fig. 4.2 λ6cm map of 1857+566 from Saikia et al. (1983), and contour plot of the model fit, with levels chosen to match those of the observed map.

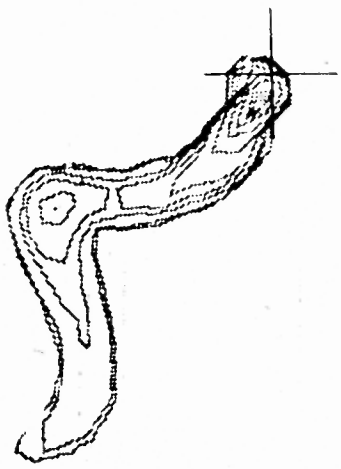

(b)

to the asymmetric source 1857+566 (Saikia et al. 1983). Fig.4.2a shows a 6 cm map of the high redshift (z=1.595) quasar 1857+566 (Saikia et al. 1983). The western lobe appears relaxed, with a warmspot, while the eastern part of the source consists of a long jet which exhibits a gradual curvature in the initial (E1) and final (E4) portions but bends sharply twice (E2 and E3) by almost 90° in opposite directions at about 7.4 arcsec from the optical quasar. The position of the quasar appears displaced from the peak of radio emission in component E1 by about one arcsec. Although this displacement is not very significant, the peak is about 28 percent polarized and is thus more likely to be a knot in the jet than the core. This has since been confirmed by Owen & Puschell (1984).

To attempt a model of 1857+566 within the framework of precessing relativistic beams, first note that the NW warmspot and the low-brightness region at the end of the jet have similar surface brightnesses and are roughly symmetrically located on opposite sides of the quasar. It is clear that it would not be possible to model both the NW warmspot and the jet. We have therefore attempted to model only the jet, ignoring the NW warmspot. As described above in section 4.1, the intensity distribution of the fluid elements in the beam has been modelled by assuming their flux densities to be inversely proportional to their proper ages, and their width to vary as the square root of proper age.

Although in this simple model the most reasonable fit is obtained by choosing $\beta \cong 0.8\text{-}0.9$, $\psi \cong 5°$, $i \cong 20°$ and about 1½ turns of the central engine precessing with $P \cong 10^4$ yr (see Fig. 4.2b), it is not very satisfactory. It is difficult to reproduce the overall morphology of the jet with both the sharp bends of similar intensity seen at E2 and E3. Further, the fit requires a small angle of inclination of the jet axis to the line of sight. This is unlikely for 1857+566 as it lies close to the upper envelope of the angular size-redshift diagram and hence is expected to be inclined at a large angle to the line of sight. This argues against a Doppler interpretation for the asymmetric nature of the jet. In addition, the small change in surface brightness over the region where the jet bends sharply suggests that the flow velocity is not large. However, the displacement of the optical quasar position from the radio peak in component E1 is very well reproduced by the model.

Saikia et al. (1983) have ruled out two other possible explanations for the structure of the jet. Bending due to Kelvin-Helmholtz instabilities is unlikely since the equipartition pressure in the jet is much greater than the pressure derived from X-ray observations of rich clusters of galaxies. Bending due to motion of the external medium is also unlikely since a 70° bend by a 10^3 km/s medium requires few particles per cc in the medium, which is again much greater than the densities in rich clusters derived from X-ray observations.

Moreover, the second sharp bend at E3 (Fig. 4.2a) is in a direction opposite to that at E2, which would require a sudden change in the external wind direction even if bending by such a wind was possible. It is conceivable that the beam may be bent by collisions with dense clouds embedded in the intergalactic medium, albeit rather fortuitously placed to cause the bends at E2 and E3.

CHAPTER FIVE

IPS OBSERVATIONS OF OOTY OCCULTATION RADIO SOURCES

5.0 In the uniform relativistic world models (i.e., the big bang models) the (observed) radio source population extends back to about 90 percent of the present age of the universe (e.g., the look-back-time for $z = 3$ is 89 percent of the present age $\frac{2}{3} H_o^{-1}$ in the Einstein-de Sitter world model). Successful models to fit the source counts (see section 6.0) require that weaker sources (tens of mJy at 408 MHz) are also cosmologically more distant (Wall, Pearson & Longair 1980, Peacock & Gull 1981). This is also supported by the observed relations between angular size and flux density (Swarup 1975, Kapahi 1975, Kapahi & Subrahmanya 1982) and percentage identification and flux density (Swarup, Subrahmanya & Venkatakrishna 1982). Hence the study of extragalactic radio sources to low flux densities is of considerable cosmological importance.

On the other hand, to understand the origin and evolution of a radio source, the structure of radio sources of various sizes on all size scales should be known. We present a study of two samples of weak radio sources from the Ooty lunar occultation survey (see section 3.0) in order to determine the fine structure in sources of different overall angular sizes. The first sample consists of sources stronger than 1 Jy at 326.5 MHz and of angular sizes between 1 and 4 arcsec.

The second contains sources of all angular sizes stronger than 0.75 Jy at 326.5 MHz. The sources were observed with the Ooty radio telescope using the method of interplanetary scintillations (IPS).

The Ooty radio telescope operating at 326.5 MHz (91.8cm) is particularly suited for IPS observations because of its large collecting area and ability to track continuously. Using the IPS method, the Ooty radio telescope can detect compact structure (0.02 to 1 arcsec) as weak as 0.05 Jy. The method of IPS is, however, insensitive to any structure on a scale $\geq$ 1 arcsec at 326.5 MHz. We briefly describe the theory behind the method (section 5.1), the observation and reduction procedure (section 5.2) and then go on to describe the results for the two samples of sources and their implications (rest of the chapter).

5.1 IPS THEORY IN BRIEF Interplanetary scintillation is the random variation in the intensity of a radio source when it is observed through the solar wind (that is, the interplanetary medium). The scintillation occurs because the radio waves from a source pass through irregularities of electron density (and therefore of refractive index) in the outer part of the solar corona and the solar wind. If a Gaussian spectrum is assumed for the irregularities, it can be specified by their scale size 'a' of about 100 km. The irregularities produce a diffraction pattern on the ground. (We model the solar wind plasma as a thin screen, see Fig.5.1.)

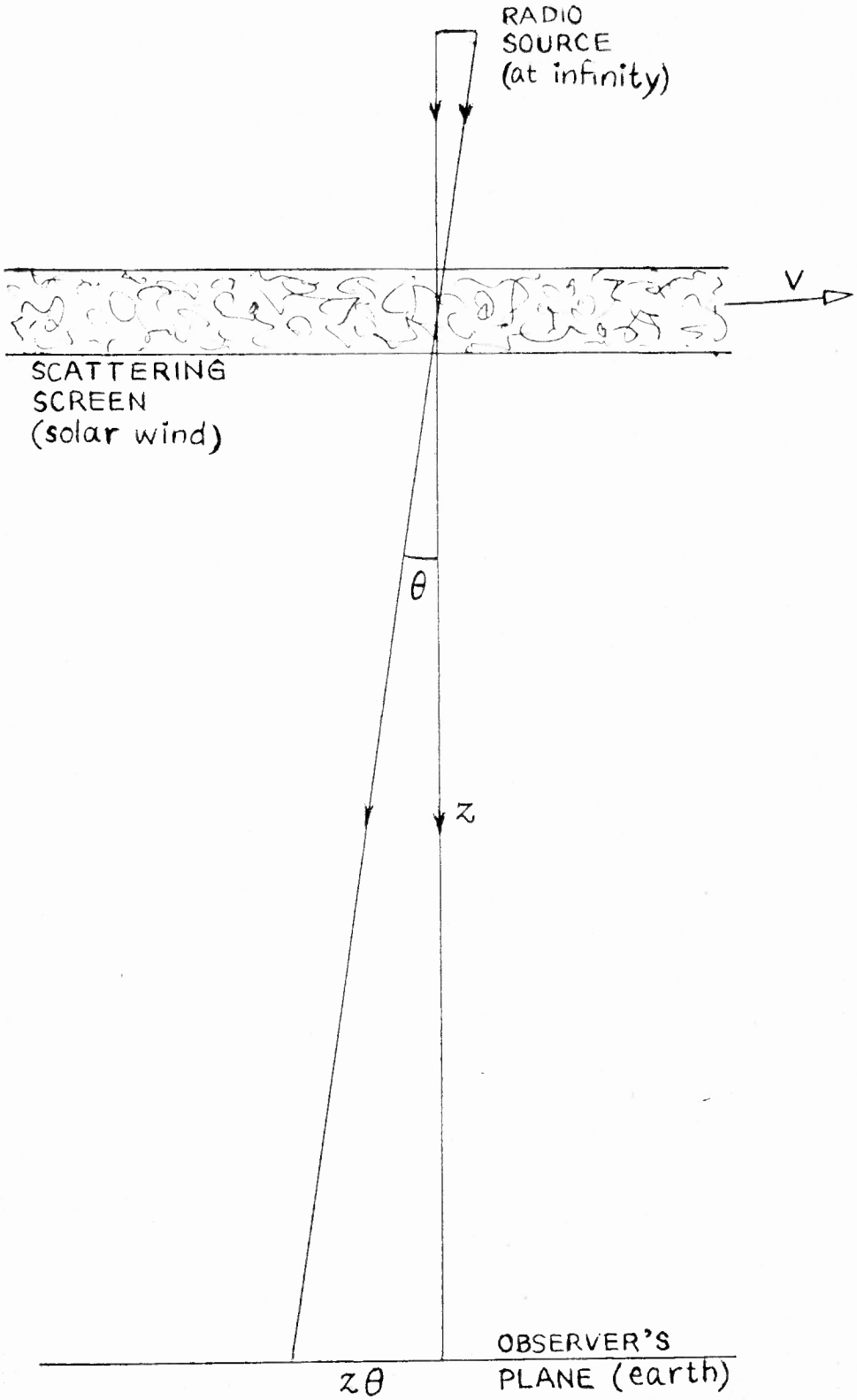

Fig. 5.1 Thin screen model for the scattering of radio waves by the interplanetary medium

The pattern drifts on the ground as the solar wind flows at a speed of about 400 km/s outward from the sun at a distance Z of about 1 AU. Each point in the source produces its own diffraction pattern. If the patterns produced by two points in the source are displaced by less than the scale of the irregularities ($a \cong 100$ km), scintillations are observed. For this the source must have an angular size roughly given by $\psi \lesssim a/Z \cong 1$ arcsec. However, the maximum angular size beyond which scintillations are washed out increases slowly with the wavelength, roughly as the square-root. The technique is easy and rapid to apply and does not need elaborate instrumentation. We give below a simplified derivation of the relation between the source brightness distribution on the sky and the statistical properties of the scintillation pattern. For a detailed exposition of IPS theory, see Pramesh Rao (1975) and references therein.

Note first that the phases of the waves that interfere to produce the scintillation pattern ~~platform~~ are lost. All the information is then contained in the power spectrum of the intensity variations, i.e., the relative strengths of variations on the various time scales. There is a simple way to relate this power spectrum to the brightness distribution of the source being observed. Referring to Fig. 5.1, let the Fourier component at spatial wavelength# λ of the intensity pattern on the ground produced by a unit point source be $I(2\pi/\lambda)$. For

a point source at θ, a phase factor $\exp(-i2\pi Z_\theta/\lambda)$ is introduced, so the Fourier component becomes

$$I(2\pi/\lambda).\exp(-i2\pi Z\theta/\lambda),$$

a shift of the pattern on the ground by $Z\theta$. Since the solar wind moves at a speed $v(\cong 400$ km/s), the pattern shifts at a frequency f such that $\lambda f = v$. For a brightness distribution $b(\theta)$ in the sky, the Fourier transform of the intensity pattern is

$$\int_{-\infty}^{\infty} I(2\pi/\lambda).\ \exp(-i2\pi(Z/\lambda)\theta).\ b(\theta)\ d\theta$$

$$= I(2\pi/\lambda)B(Z/\lambda) = I(2\pi f/v)\ B(Zf/v),$$

in which $B(s=Zf/v)$ is the Fourier transform of $b(\theta)$:

$$B(s) = \int_{-\infty}^{\infty} b(\theta)\exp(-i2\pi s\theta)\ d\theta .$$

By definition, the power spectrum is the square of the Fourier transform. So the power spectra of an extended source of brightness distribution $b(\theta)$ and of a unit point source are related by

$$P_{extd}\ (f) = P_{pt}(f).|B(Zf/v)|^2.$$

Inverting this relation, we get

$$|B(s)| = \sqrt{P_{extd}\ (vs/Z)\ /\ P_{pt}\ (vs/Z)}.$$

Thus, in principle, the IPS power spectrum of an extended source contains information on the amplitudes, but not the

phases, of the Fourier transform of the brightness distribution of the source upto a maximum spatial frequency (or baseline, in interferometry parlance) s_{max}. In principle, this is similar to the information obtained from the early VLBI experiments. However, it is difficult, in practice, to rely too much on the power spectrum due to the uncertainties of the solar wind and various other sources of error. Instead of using the whole power spectrum only its width and the area under it are used to derive two important parameters for the sources, viz., the fraction of flux density in the scintillating component (μ) and its angular size (ψ) as described in the next section.

5.2 IPS OBSERVATION AND REDUCTION PROCEDURE The method used for our observations and the reduction procedure adopted were, in general, similar to the method used for the earlier IPS survey at Ooty (Pramesh Rao et al. 1974). Briefly, the source was tracked continuously for about 20 min and an adjacent patch of cold sky for about 5 min immediately after or (less often) before the 'on-source' track. The 'off-source' track can, in principle, be used to get the total flux density of the source by subtracting the off-source level from the on-source level, but we have not done this since most of our sources are weak in comparison with the confusion limit of the Ooty radio telescope ($\simeq$1.5 Jy). Instead, we have used the flux densities given in the lunar occultation surveys (see

section 3.0) which are not seriously affected by confusion. A relatively strong (≥8 Jy) flux calibration source from the standard list was also observed in the same way, except that the on-source track also lasted for about 5 min. For a short run of IPS observations (~3 hours), only one flux calibration was done. Two or three such calibrations were done for a longer session (~8 hours). A receiver bandwidth of 4 MHz was used and the output from a correlated channel, which is the result of multiplying the voltage signals from the north and south halves of the telescope (Swarup et al. 1971), smoothed using an RC time constant of 50 ms, was recorded digitally on magnetic tape at the rate of 50 samples/sec. This output, which consists of the intensity fluctuations of the source, along with correlated channel outputs for several adjacent beams and one total power channel output for a far off beam were also fed to a chart recorder for the purpose of monitoring ionospheric scintillations, thunderstorms, local interference from the vicinity of the telescope, etc. Each type of unwanted noise has a characteristic signature (as the Ooty radio telescope has 12 adjacent beams, it is easy to recognize interference) and the charts were marked accordingly as the observation proceeded. These were later used to edit out unwanted blocks of data, more blocks having been acquired to make up for this loss. The data on the magnetic tape were later reduced using programs specially written for the purpose with the PDP 11/70 timesharing system.

In what follows, we briefly describe what these programs do. Running means over 512 data points are subtracted to remove any drifts and the variance of the data is then computed. The power spectrum is also computed using a 2048-point fast-Fourier algorithm. The spectra of successive minutes of data are cumulatively added. This integrated power-spectrum is corrected for the attenuation caused by the time-constant circuit (Pramesh Rao 1975, pp.100-6). The power spectrum thus calculated is stored on another magnetic tape and used later for making plots through the last of the reduction programs. These power spectrum plots give, among other things, the mean, the variance and the first and second moments of the power spectrum for each track. There are several consistency checks built into the programs.

The dedicated on-line computer Varian 620/i, which was used for data acquisition, produced blockwise means and variances and also power spectrum plots as the observation went on. An older version of the reduction programs, using a 1024-point fast-Fourier algorithm, was used in real time for this purpose. These plots can be used for analysis if there are no blocks with serious interference, and were useful when the data on tape got erased or were not written properly due to tape unit malfunction or any other such problem. The scintillation index, m, which is the area under the power spectrum profile normalized to the flux density of the source,

and the second moment f_2, which is a parameter indicating the width of the power spectrum, were calculated for each observation.

Each source was observed in this way on several days corresponding to different angular separations (= elongations ε) from the Sun, ranging from about 6° to 25° for most sources and upto 40° for a few. To find the equivalent size ψ of the scintillating component, values of f_2 are plotted against $\sin\varepsilon$ on a log-log graph sheet and compared with model calculations (Pramesh Rao et al. 1974). The model consists of a Gaussian brightness distribution of FWHM ψ for the scintillating component and a Gaussian power spectrum for electron density fluctuations in the interplanetary medium. Although the observed power spectrum appears to be more complex than any such idealized form (Ananthakrishnan & Kaufman 1982 and references therein), a Gaussian distribution has been assumed since it is adequate for the purpose. The normalization of the model log f_2-log $\sin\varepsilon$ curves was done using extensive observations of a few well-studied calibration sources known to have sizes of few tens of milliarcsec at metre-wavelengths (Pramesh Rao 1975, Ananthakrishnan 1976).

The fraction of the total flux density in the scintillating structure (that is, the compactness parameter μ) was estimated in the following manner. The scintillation index m is given by $m = (\sigma_{ON} - \sigma_{OFF})/I$ where σ_{ON} and σ_{OFF} are the

on-source and off-source rms values and I the mean intensity. Alternatively, it is the area under the power spectrum of the scintillations. The compactness parameter μ is then estimated by taking a weighted average of the ratios m/m_o of the source scintillation index m (corrected for the measured component size assuming an equivalent circular Gaussian) to the scintillation index m_o of the calibrating source at the same elongation:

$$\mu_{\text{corrected}} = \mu_{\text{weighted mean}} \left[1+0.36(7.5\psi/\text{arcsec})^2\right]^{\frac{1}{2}}.$$

In estimating μ, only observations in the weak scattering regime ($\varepsilon \gtrsim 14°$ at 326.5 MHz) were used. ψ and μ are thus two independent parameters describing the structure of the source.

5.3 THIRTY SOURCES OF SIZES OF FEW ARCSEC: OBSERVATIONS As stated at the beginning of this chapter (section 5.0), the study of extragalactic radio sources on all scale sizes is important for understanding their origin and evolution. Extended sources (tens of arcsec) have been extensively mapped using aperture synthesis, and compact sources (tens of milliarcsec) with very long baseline interferometry (VLBI). Sources with intermediate sizes (a few arcsec), however, are only now being mapped (e.g. by MERLIN in UK and VLA in USA). We observed two samples of radio sources from the Ooty occultation survey for fine structure, using the method of IPS (see sections 5.1 and 5.2 above). Observations of a sample of 30 sources with sizes of few arcsec are described in this section, and of another

sample of 90 in section 5.4.

The 30 source sample was formed from the Ooty lunar occultation survey (section 3.0) by Gopal-Krishna, Preuss & Schilizzi (1980) for 4996 MHz single baseline VLBI observations. Exclusion from the occultation lists 1-9 of all sources with $S_{326.5} < 1$ Jy and $\delta < -25°$ leaves a sample of 266 sources (Gopal-Krishna, Preuss & Schilizzi 1980) of which 30 have sizes between 1 and 4 arcsec, and occultation scans along position angles differing by at least 20°. The median flux density of these 30 sources is 1.75 Jy. Both, the sample of 266 sources and its subsample of 30 sources have identification rates very similar to the 4C complete sample ($S_{178} > 2$ Jy; Pilkington & Scott 1965, Gower et al. 1967). We decided to observe this sample of 30 sources with IPS to compare any fine structure at 326.5 MHz with the high-frequency structure found by Gopal-Krishna et al. (1980) who carried out VLBI observations at 4996 MHz using the Effelsberg-Westerbork baseline which provided fringe-spacings in the range 0.05 to 0.125 arcsec.

Suitable observation dates were determined from solar plots where the positions of these sources (as well as of those from the other sample of 90) were marked. The solar elongation ε of a source (defined as the sun-earth-source angle) on a given date could be simply read off the solar plot to facilitate the scheduling. Most of the observations were made in 1981, though there are a few from earlier years and a few

(...5-17)

Table 5.1 Observation log for the 30 sources

Source	Date	sinε	μ? †	ψ? †	Date	sinε	μ? †	ψ? †
1	2	3	4	5	6	7	8	9
0011+054	09.04.81	0.248	y	y	03.03.82	0.398	y	y
	10.03.82	0.286	y	y	13.03.82	0.237	y	y
	15.03.82	0.205		y	18.03.82	0.157		y
0057+105	14.03.82	0.422	y	y	18.03.82	0.359	y	y
	21.03.82	0.312	y	y	26.03.82	0.231		y
	28.03.82	0.199		y				
0352+210	03.05.81	0.318	y	y	07.05.82	0.257	y	y
	09.05.82	0.225		y				
0405+258	03.05.81	0.387	y		10.05.81	0.280	y	y
	14.06.81	0.322	y		29.05.82	0.098		y
	30.05.82	0.106		y				
0410+266	06.06.81	0.186		y	14.06.81	0.304	y	y
	15.05.82	0.231		y				
0500+270	24.06.81	0.271	y	y	28.06.81	0.333		y
	19.05.82	0.342	y	y	22.05.82	0.296	y	y
	01.06.82	0.144		y				
0632+189	06.06.81	0.395	y	y	12.06.81	0.304	y	y
	24.06.81	0.124		y	10.07.81	0.181		y
	18.07.81	0.304	y	y	24.07.81	0.395	y	y
0646+184	12.06.81	0.359	y	y	24.06.81	0.177		y
	28.06.81	0.122			10.07.81	0.133		
	20.06.82	0.241	y	y	25.06.82	0.166		y
	30.06.82	0.102		y	10.07.82	0.129		y
	14.07.82	0.186						
0656+213	23.06.81	0.212		y	24.06.81	0.196		y
	28.06.81	0.131		y	27.07.81	0.347	y	y
0706+261	14.06.81	0.385	y	y	24.06.81	0.230		y
	28.06.81	0.168		y	20.06.82	0.297	y	y
	13.07.82	0.107		y	16.07.82	0.151		y
0710+241	18.07.81	0.157		y	21.07.81	0.205		y
	25.07.81	0.269	y	y	27.07.81	0.301	y	y

contd...

Table 5.1 contd....

1	2	3	4†	5†	6	7	8†	9†
0736+167	24.06.81	0.370	y	y	03.07.81	0.233		
	11.07.81	0.120		y	22.07.81	0.127		y
	25.07.81	0.168		y	30.06.82	0.282	y	
	02.07.82	0.252	y					
0746+162	24.06.81	0.406	y		28.06.81	0.346	y	y
	03.07.81	0.270	y	y	11.07.81	0.152		y
	24.07.81	0.122		y				
1055+018	15.08.81	0.396	y	y	18.08.81	0.350	y	y
	26.08.81	0.227		y	28.08.81	0.197		y
	30.08.81	0.167		y	02.09.81	0.125		y
	25.09.81	0.300	y	y	27.09.81	0.332	y	y
	29.09.81	0.363	y	y				
1123+012	26.08.81	0.326	y	y	29.08.81	0.278	y	y
	02.09.81	0.213		y	05.09.81	0.165		
	03.10.81	0.315	y	y	07.10.81	0.379	y	y
1159-060	29.08.81	0.463		y	02.09.81	0.404	y	y
	06.09.81	0.343	y	y	15.09.81	0.207	y	y
	14.10.81	0.322	y	y	16.10.81	0.353	y	y
	18.10.81	0.384	y	y	20.10.81	0.415	y	y
	21.10.81	0.430	y	y	22.10.81	0.445	y	y
	23.10.81	0.460	y	y	25.10.81	0.490	y	y
	28.10.81	0.534	y	y	30.10.81	0.563	y	y
	31.10.81	0.577	y	y	10.11.81	0.709	y	y
	11.11.81	0.721	y	y	13.11.81	0.745	y	y
	15.11.81	0.768	y	y				
1304-101	23.10.80	0.192		y	24.10.80	0.209		y
	26.10.80	0.242	y	y	30.10.80	0.307	y	y
	31.10.80	0.324	y	y	04.11.80	0.388	y	y
	18.09.81	0.411	y	y	27.09.81	0.269	y	
	30.09.81	0.220		y	04.10.81	0.156		y
1348-129	06.11.80	0.237		y	07.11.80	0.254		y
	05.10.81	0.318	y	y	08.10.81	0.269	y	
	10.11.81	0.299	y	y	20.11.81	0.461	y	y
	21.11.81	0.477	y	y	24.11.81	0.522	y	y
	27.11.81	0.567	y	y	29.11.81	0.596	y	y
	02.12.81	0.637	y	y	05.12.81	0.677	y	y
	07.12.81	0.703	y	y	12.12.81	0.763	y	y
	17.10.82	0.113		y				

contd...

Table 5.1 continued...

1	2	3	4†	5†	6	7	8†	9†
1350-154	09.10.81	0.283	y	y	13.10.81	0.218		y
	13.11.81	0.280	y	y				
1456-165	23.10.80	0.295	y	y	24.10.80	0.279	y	y
	25.10.80	0.262	y	y	26.10.80	0.245	y	y
	31.10.80	0.160		y	22.11.80	0.224		y
	26.11.80	0.292	y	y				
1632-199	18.12.80	0.282	y	y	20.12.80	0.315	y	y
	23.12.80	0.365	y	y	10.11.81	0.384	y	y
	09.12.81	0.124		y	12.12.81	0.175		y
1924-193	18.12.81	0.414	y	y	20.12.81	0.382	y	y
	25.12.81	0.299	y	y	28.12.81	0.248	y	y
	03.01.82	0.147		y				
2019-202	04.01.82	0.335	y	y	06.01.82	0.301	y	y
	08.01.82	0.267	y		05.02.82	0.225		y
	07.02.82	0.259	y	y	10.02.82	0.310	y	
2023-142	04.01.82	0.381	y	y	07.01.82	0.333	y	y
	10.01.82	0.284	y	y	13.01.82	0.236	y	y
	17.01.82	0.173		y	05.02.82	0.204		y
2050-188	15.02.74	0.272	y	y	09.02.75	0.164		y
	18.02.75	0.318	y	y	07.02.79	0.129		y
	10.02.79	0.181		y	07.01.82	0.406	y	y
	10.01.82	0.357	y	y	13.01.82	0.307	y	y
	07.02.82	0.133		y	14.02.82	0.254	y	y
2058-179	13.01.74	0.341	y	y	19.01.74	0.239	y	y
	14.01.82	0.326	y	y	17.01.82	0.275	y	y
	10.02.82	0.148		y	12.02.82	0.200		y
	16.02.82	0.251	y	y				
2243-032	09.02.74	0.375			15.02.74	0.278		
	18.02.75	0.234		y	21.02.75	0.186		y
	08.03.79	0.120		y	15.03.79	0.226		y
	08.02.81	0.388	y	y	05.02.82	0.440		y
	09.02.82	0.376	y	y	10.02.82	0.360	y	y
2245-022	08.02.81	0.404	y	y	19.02.82	0.232		y
	25.03.82	0.378	y	y				

contd....

Table 5.1 continued ...

1	2	3	4†	5†	6	7	8†	9†
2257-048	16.03.79	0.188			21.03.79	0.271	y	
	19.02.82	0.246	y	y	17.03.82	0.208		y
2335+031	21.02.79	0.420	y	y	24.02.79	0.373	y	y
	05.03.79	0.231		y	07.03.79	0.200		y
	23.03.79	0.136		y	25.03.79	0.162		y
	26.03.79	0.177			07.04.79	0.361	y	y
	08.04.79	0.377	y	y				

† 'y' in columns μ? and ψ? indicates that the observation was used to derive the values of μ and ψ respectively. A blank indicates that it was not used.

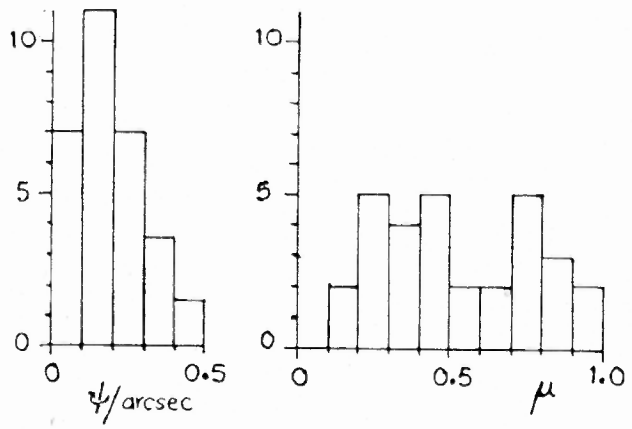

Fig. 5.2 Observed distributions of the compactness parameter μ and the (mean) angular size of the compact structure ψ for the 30 few arcsec sources

(5-11 ...)

in 1982 (see Table 5.1 for details).

In Table 5.2, we have given the values of μ and ψ for the 30 sources, together with their structures, sizes and flux densities at 326.5 MHz, as well as the optical identification data, all taken from the published Ooty lunar occultation lists. Also tabulated is the spectral index α_{327}^{4996} (see section 1.2) between 326.5 MHz and 4996 MHz given by Gopal-Krishna et al. (1980). The spectral class as defined in the next section is also tabulated. Histograms of μ and ψ are shown in Fig. 5.2. It is seen that about 45 percent (which is the median value of μ) of the total flux density at 326.5 MHz arises from scintillating fine structure between 0.05 and 0.5 arcsec in size with a median value of 0.18 arcsec. The remainder of the emission should arise from more extended structure to which our IPS observations are not sensitive. Since the total spectra of the sources are steep ($\alpha_{327}^{4996} \geq 0.5$; see section 1.2) and the IPS component has typically 45 percent of the flux density at 326.5 MHz, the typical IPS component is also expected to have a steep spectrum.

5.3.1 Interpretation The nature of steep-spectrum sources with sizes of a few arcsec at metre-wavelengths is not well understood. Low luminosity radio sources are generally identified with normal spirals, Seyferts and also ellipticals, but the high luminosity radio sources are mostly identified with bright active ellipticals. Most of the high luminosity steep-

Table 5.2
Data for the 30 sources.

Source	Optical identification*	S_{327} (Jy)	Radio structure/size				α_{327}^{4996}	Class
			Overall† (arcsec)		Scint. Comp. (arcsec)			
					μ*	ψ*		
0011 + 054	EF	4.2	D	3.5	0.17(4)	0.27(6)	0.93	A
0057 + 105	EF	1.0	S	1.7	0.46(3)	0.36(5)	0.68	B
0352 + 210	18 mag NSO	3.3	S	2.7	0.22(2)	0.05(3)	0.87	A
0405 + 258	EF	1.0	S	2.0	0.30(3)	0.10(3)	0.85	A
0410 + 266	EF	2.1	D	3.0	0.62(1)	0.20(3)	1.15	A
0500 + 270	Cwd	1.2	S	3.5	0.44(3)	0.10(5)	0.76	B
0632 + 189	EF	3.0	PD	1.5	0.51(4)	0.12(6)	1.20	A
0646 + 184	EF	1.4	S	3.0	0.47(2)	0.10(6)	0.97	A
0656 + 213	19 mag G	2.4	S	1.5	0.36(1)	0.05(4)	1.12	A
0706 + 261	21 mag RO	2.5	D	3.5	0.18(2)	0.17(6)	0.65	B
0710 + 241	18.5 mag NSO (Cwd)	1.2	S	3.6	0.30(2)	0.25¶(4)	1.05	A
0736 + 167	EF	1.8	D	4.0	0.72(3)	0.25¶(4)	1.16	A
0746 + 162	EF	1.4	PD	3.4	0.83(3)	0.13¶(4)	0.89	A
1055 + 018	18 mag Q	4.0	D	1.5	0.72(5)	<0.02(9)	0.14	B
1123 + 012	20 mag G, cl	1.2	PD	3.5	0.47(4)	0.28(5)	0.70	B
1159 – 060	EF	1.9	S	1.6	0.87(18)	0.15(19)	0.90	A

contd....

Table 5.2 (continued)

1304 – 101	EF	1.4	S	4.0	0.71(6)	0.14(9)	0.98	A
1348 – 129	EF	3.5	EXT	‡	1.00(12)	0.15(14)	0.95	A
1350 – 154	EF	1.0	S	3.0	0.31(2)	0.20(3)	1.16	A
1456 – 165	21 mag BO	1.5	S	3.0	0.48(5)	0.10(7)	0.79	B
1632 – 199	EF	1.0	S	3.5	0.95(4)	0.15(6)	1.02	A
1924 – 193	Cwd	1.1	PD	2.8	0.63(4)	0.05(5)	0.99	A
2019 – 202	EF	1.2	S	2.0	0.75(5)	0.02(4)	0.51	B
2023 – 142	EF/20 mag G	1.0	S	2.7	0.35(4)	0.30(6)	1.29	A
2050 – 188	EF	2.1	D	2.6	0.55(6)	0.30(10)	1.02	A
2058 – 179	19.5 mag BSO?	3.5	S	3.3	0.28(5)	0.20(7)	0.90	A
2243 – 032	19 mag BO, G?	3.5	EXT	§	0.72(3)	0.20(8)	0.74	B
2245 – 022	EF	1.25	D	3.5	0.81(2)	0.40(3)	0.60	B
2257 – 048	EF	1.5	S	2.2	0.22(2)	0.35(2)	0.78	B
2335 + 031	18 mag BL Lac	4.3	S	2.0	0.29(4)	0.42(8)	0.75	B

Notes

* EF, empty field; NSO, neutral stellar object; Cwd, crowded field; G, galaxy; RO, red object; Q, quasar; BO, blue object; BSO, blue stellar object.

† D, Double; S, Single; PD, probable double; EXT, extended.

‡ Most of the flux in compact component, aboue 15 per cent in 5 arcsec extension in PA 150°.

§ 60 per cent in compact component, remaining in 5 arcsec SW extension.

¶ Scintillating structure is complex.

* Number in parentheses is the number of observations used to derive the value.

spectrum sources are extended. But some may appear small either because they are intrinsically small and/or more distant or because they are actually large and linear, but seen end-on. Since 60 percent of the sources are empty fields to the PSS limit (see Table 5.2), their redshifts z are probably $\gtrsim 0.5$ (Swarup, Subrahmanya & Venkatakrishna 1982). The θ-z (angular size - redshift) relation for a given linear size starts saturating to a lower θ-limit by this redshift for the uniform relativistic world models. Hence the effect of the actual linear sizes being small at earlier epochs (larger z) (Kapahi 1975a,b) is important in determining the observed angular sizes#.

Gopal-Krishna, Preuss & Schilizzi (1980) conclude that most of the 30 sources detected with VLBI by them at 5 GHz are doubles seen end-on and that they see flat-spectrum nuclear cores enhanced by relativistic beaming. Although this may be true for the sources 1055+018 ($\alpha_{327}^{4996} = 0.14$) and 2019-202 ($\alpha_{327}^{4996} = 0.51$) which have flatter spectra, the spectra of all the other sources are steep. This is in contrast to the relatively flat spectra normally found in samples of core-dominated sources (e.g., Kapahi 1981, Perley 1983). It is unlikely that all the present 30 sources fall into any one category. By comparing their low and high frequency structures, we attempt below a general classification of these sources.

To compare meaningfully the IPS and VLBI results, one

must appreciate the differences in the two techniques. The size and flux density given by IPS refer to weighted averages over all the compact components present in the sources; if there are many compact components, IPS cannot distinguish between them. Single baseline short duration VLBI, on the other hand, samples only the structure on the scale of the fringe spacing FS, so that a unique source model is not possible. In particular, these VLBI observations cannot distinguish between a point source (that is a source of size $<<$FS) and a source of size $\leq$ FS.

Our IPS observations show scintillating components of $\mu \geq 0.17$ (Table 5.2) in each of the 30 sources, whereas Gopal-Krishna, Preuss & Schilizzi (1980) could detect VLBI correlated flux in only 21 of them. For the remaining nine they set upper limits of 30 m Jy. They assumed that the detected VLBI correlated flux came from flat-spectrum nuclear components which are unresolved, allowing them to calculate the core-fraction by assuming that the correlated flux is independent of FS. The IPS sizes cover a wide range and clearly do not refer to such small components. This may imply that the IPS and VLBI components are physically different. However, since the VLBI fringe spacings cover only a narrow range (making the VLBI observations essentially single baseline measurements), it is not clear how valid is the assumption that the VLBI components are unresolved.

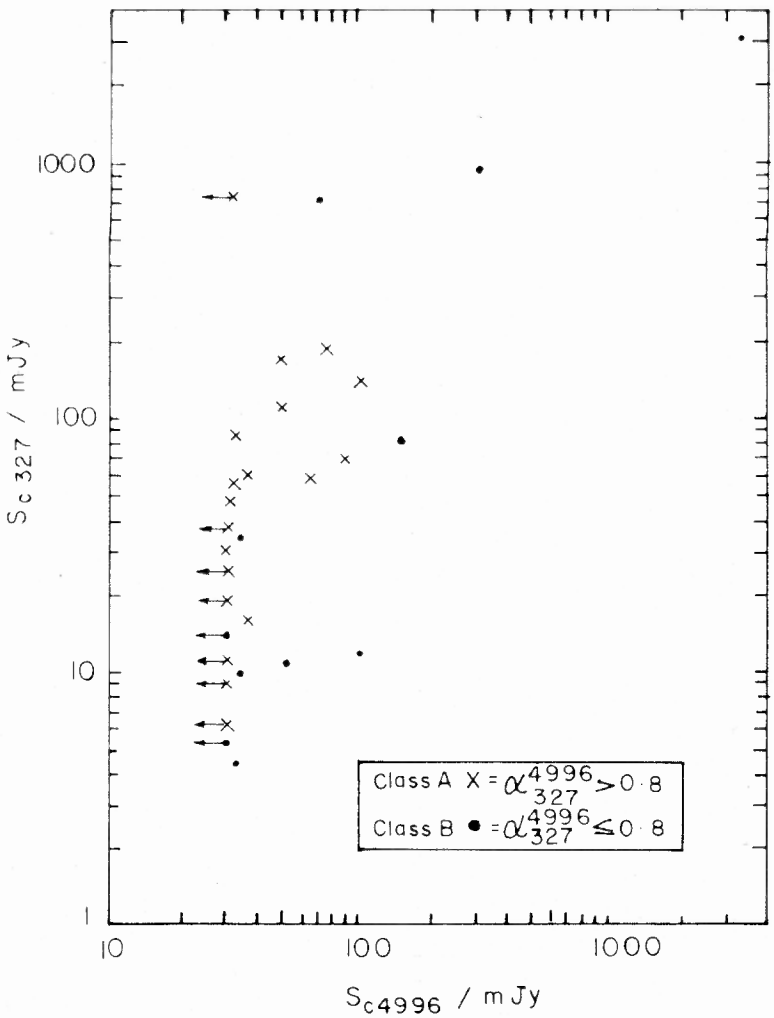

Fig. 5.3 A log-log plot of S_{c327} vs S_{c4996} (see text for details)

To test the possibility that the IPS and VLBI measurements refer to the same structure, we have made the following calculation. Assuming that the 326.5 MHz compact component is a uniform disc of diameter ψ, its visibility is given by

$$S_o \, J_1(\pi\psi/FS) / (\tfrac{1}{2}\pi\psi/FS)$$

where S_o is the flux density of the compact component, taken to be μS_{327} and J_1 a Bessel function. To eliminate the oscillatory behaviour of the visibility, we have, for small FS, replaced the Bessel function by the average of its modulus, which gives us

$$S_{c327} = (4\sqrt{2}/\pi^3) \; (\mu S_{327}) (FS/\psi)^{3/2}$$

for the predicted correlated flux density for an assumed VLBI experiment at 326.5 MHz. We have used this formula to estimate S_{c327} for each source at the Effelsberg-Westerbork VLBI fringe spacing FS. For four sources, FS was greater than ψ and the above formula does not apply. The predicted correlated flux density was then taken to be μS_{327}. A Gaussian model was not used for the compact component since the model visibility is then very insensitive to μ but much more sensitive to ψ.

A plot of S_{c327} vs S_{c4996} (the VLBI correlated flux at 5 GHz) is presented in Fig. 5.3. The sources for which there is no VLBI detection are shown as upper limits at S_{c4996} = 30mJy. The plot shows a definite, though weak, correlation, which is

Table 5.3 % VLBI detections for different ranges of the predicted 326.5 MHz correlated flux density

S_{c-327} - range (mJy)	No. of sources	Median S_{c327} (mJy)	Percentage VLBI detections
<20	11	11	45
20 to 80	9	50	78
>80	10	170#	90

This value equals 10** (median of log S_{c327}).

brought out more clearly in Table 5.3 where we have tabulated the percentage of VLBI detections against the median S_{c327} for the three ranges $S_{c327} < 20$ mJy, $20 < S_{c327} < 80$ mJy and $S_{c327} > 80$ mJy. The table shows that there is a higher fraction of sources not detected by the VLBI experiment where the predicted S_{c327} is low. With a more sensitive VLBI experiment, the points corresponding to undetected sources would only shift to the left in Fig. 5.3, strengthening the correlation. This correlation is hard to understand if the IPS and VLBI components refer to different physical features with uncorrelated emission, implying that, statistically, either the VLBI component at 5 GHz and the IPS componetn at 327 MHz originate

in the same physical structure, or, if different, the emission from the two features is correlated.

A tight correlation between S_{c327} and S_{c4996} implies a certain spectral index for the compact structure. However, the value of the inferred spectral index depends on the absolute S_{c327} values, i.e., the vertical scale in Fig. 5.3. We refrain from deriving any such spectral index from Fig.5.3 because (i) the correlation is not tight and (ii) the vertical scale on which S_{c327} values fall is highly model-dependent; the assumption of different models for the compact component gave different vertical scales, but the correlation did show up in each case.

To study further the nature of the compact components in the 30 sources, we have divided them into two spectral classes. Those with steeper spectra ($\alpha_{327}^{4996} > 0.8$) are plotted as crosses (class A) in Fig. 5.3 and the others as dots (class B). Since almost all the sources in the sample have steep spectra ($\alpha_{327}^{4996} > 0.5$), this division at $\alpha_{327}^{4996} = 0.8$ has been made only to see general trends. Examining the properties of the two classes (see Table 5.4) we find that: (i) of the 11 sources in class B, nine were detected with VLBI in contrast to 12 out of 19 for class A. In addition, of the four sources detected by VLBI from those with $S_{c327} < 20$ mJy, three are in class B. This higher VLBI detection rate for class B

Table 5.4 % VLBI detections and % optical identifications for the two spectral classes

Spectral class	No. of srcs	% VLBI detections	% op.ids.
A: $\alpha_{327}^{4996} > 0.8$	19	63	16
B: $\alpha_{327}^{4996} \leq 0.8$ (but $\gtrsim 0.5$)	11	82	55

suggests that the spectrum is less steep due to a large contribution from a relatively flat-spectrum compact component. (2) Six sources are optically identified out of the 11 in class B (rate 55 percent) compared to only three out of the 19 of class A (16 percent). This is consistent with the high fraction of identified flat-spectrum sources in high-frequency catalogues (see e.g. Wall, Shimmins & Merkelijn 1971; Pauliny-Toth et al. 1972). (3) The mean value of α_{327}^{4996} is virtually the same for the sources of class A which were detected with VLBI (mean 1.01) and those not detected (mean 1.04). If the VLBI detections referred to sources with flat-spectrum components, the mean spectral index would be expected to be lower. All of these points suggest that this break up of the sample is physically meaningful in that sources of class B probably

have stronger flat-spectrum compact components which are absent or weak in class A.

The compact components in class A sources could be either hotspots in outer lobes of doubles (see section 1.3) or compact steep-spectrum cores as found in many normal galaxies and low luminosity radio sources (Bridle & Fomalont 1978), powerful extended radio sources like 3C 236 (Strom & Willis 1980) and active galaxies such as Seyferts (Wilson 1982), all of which have sizes of the order of a kiloparsec. It should be noted here that what were called steep-spectrum cores have in some cases been resolved into jets and knots in jets (cf Phillips & Mutel 1981, Wilkinson 1982) or small scale doubles (Phillips & Mutel 1981). (See also van Breugel et al. 1984). We use the term 'steep-spectrum cores' to denote how these would appear at a coarser resolution such as ours. Assuming a typical redshift of $\simeq 0.3$ (Gopal-Krishna, Preuss & Schilizzi 1980), a kiloparsec translates to an angular size of ~ 0.2 arcsec (in the Einstein-de Sitter cosmology with H_o=50 km/s/Mpc), similar to the sizes measured by IPS. The structure of hotspots can be quite complex, with features as small as 150-300 pc at the outer edges (Dreher 1981; Barthel 1983). Thus, while IPS would tend to show the overall size of the hotspots, VLBI would see the more compact features. The relatively weak correlation between S_{c327} and S_{c4996} (Fig. 5.3) then probably indicates that the fractional flux density and size

of the fine structure in the hotspots vary from source to source. Although most of the sources are not found from lunar occultations to be double, it is possible that, with better resolution, a substantial fraction may turn out to be doubles or jets or knots in jets.

As said earlier, of the 11 sources in class B ($\alpha_{327}^{4996} \leq 0.8$), two have $\alpha_{327}^{4996} \leq 0.5$ and are probably flat-spectrum cores. For the other nine, the (relatively) flatter spectra could be partly due to such cores and partly due to the flatter spectrum of the youngest hotspots (section 1.3).

In conclusion, sources selected as having sizes of a few arcseconds at metre-wavelengths emit about half their flux from fine structure ~0.2 arcsec at metre-wavelengths, and show much finer structure still at centimetre-wavelengths. The fine structure at high and low frequencies probably relate to the same physical feature. For about two-thirds of the sources the fine structure probably originates either in hotspots or in steep-spectrum kiloparsec cores, and for the remainder it originates in flat-spectrum compact components or the youngest hotspots.

5.4 AN UNBIASED SAMPLE OF 90 OOTY OCCULTATION RADIO SOURCES: OBSERVATIONS The method of IPS has given information on the metre wavelength subarcsec structure of extragalactic radio sources for over one and a half decades. The three major

Table 5.5 Observation log for the 90 sources

Source	Date	sinε	μ?†	ψ?†	Date	sinε	μ?†	ψ?†
1	2	3	4	5	6	7	8	9
0045+076	15.03.82	0.344			21.03.82	0.245		
	28.03.82	0.130			Nonscintillating			
0054+078.2	13.03.82	0.408	y	y	16.03.82	0.360	y	y
	21.03.82	0.278	y	y	26.03.82	0.195	y	y
	28.03.82	0.162		y	30.03.82	0.128		y
0054+090	16.03.82	0.370	y	y	21.03.82	0.289	y	y
	26.03.82	0.207	y	y	28.03.82	0.174		y
	30.03.82	0.142		y				
0146+133	12.04.81	0.144		y	13.04.81	0.127		
	04.04.82	0.280	y	y	10.04.82	0.181		y
0153+136	09.04.81	0.220	y	y	08.05.81	0.272	y	y
	06.04.82	0.274	y	y				
0156+126	13.04.81	0.156		y	03.05.81	0.183		y
	06.04.82	0.277	y	y	10.04.82	0.211	y	y
	04.05.82	0.195	y	y				
0156+136	12.04.81	0.183		y	10.05.81	0.291	y	y
	06.04.82	0.286	y	y	10.04.82	0.220	y	y
	05.05.82	0.206	y	y				
0200+130	08.04.79	0.267	y	y	12.04.81	0.193	y	y
	03.05.81	0.163		y	10.04.82	0.230	y	y
0202+149	Observed extensively by Pramesh Rao (1975) in 1971.							
0206+136	13.04.81	0.203			03.04.82	0.371	y	y
0215+151	13.04.81	0.245	y	y	19.04.81	0.146		
	10.04.82	0.298			12.04.82	0.266	y	y
	18.04.82	0.166		y				
0232+150	13.04.81	0.310	y	y	19.04.81	0.211	y	y
0237+154	09.04.81	0.394	y	y	19.04.81	0.232	y	y
	22.04.82	0.186		y	25.04.82	0.136		
0309+175	19.04.81	0.366	y	y	26.04.81	0.253	y	y
	22.05.82	0.178		y				
0312+180	19.04.81	0.376			26.04.81	0.263		
	22.05.82	0.167			23.05.82	0.184		
	Nonscintillating							
0325+180	26.04.81	0.314	y	y	07.06.81	0.378	y	y
	04.05.82	0.188		y	25.05.82	0.165		y
0342+199	26.04.81	0.385	y	y	03.05.81	0.273	y	y
	07.06.81	0.306	y	y	07.05.82	0.212	y	y
0343+184	03.05.81	0.273	y		28.05.82	0.143		
	29.05.82	0.159			30.05.82	0.175		
	Nonscintillating?							

contd....

Table 5.5 contd...

1	2	3	4†	5†	6	7	8†	9†
0359+193	03.05.81	0.337			07.06.81	0.243		
	14.06.81	0.355	y		30.05.82	0.109		
	02.06.82	0.158		y	04.06.82	0.191	y	y
	05.06.82	0.207			11.06.82	0.303	y	y
0429+201	07.06.81	0.122			14.06.81	0.235	y	y
	24.06.81	0.392	y	y	09.05.82	0.365	y	y
	06.06.82	0.102			11.06.82	0.183		y
	13.06.82	0.215	y	y				
0436+203	14.06.81	0.208			12.05.82	0.344	y	y
0453+205	12.06.81	0.111		y	14.06.81	0.143		y
	24.06.81	0.303	y	y				
0512+209	24.06.81	0.227	y	y				
0513+198	24.06.81	0.231	y	y	04.06.82	0.123		y
	16.06.82	0.105		y				
0708+184	14.06.81	0.408			15.07.81	0.124		
	Nonscintillating							
0736+167	24.06.81	0.370	y	y	03.07.81	0.233	y	
	11.07.81	0.120		y	22.07.81	0.127		y
	25.07.81	0.168		y	30.06.82	0.282	y	
	02.07.82	0.252	y					
0746+162	24.06.81	0.406	y	y	22.06.81	0.346	y	y
	03.07.81	0.270	y	y	11.07.81	0.152		y
	24.07.81	0.122		y				
0748+164	28.06.81	0.353	y	y	04.07.81	0.261	y	y
	11.07.81	0.156			25.07.81	0.125		y
	27.07.81	0.152		y	10.07.82	0.175		y
	13.07.82	0.133		y				
0806+152	03.07.81	0.349	y	y	15.07.81	0.169		y
	07.07.82	0.292	y	y	10.07.82	0.247	y	y
0852+124	15.07.81	0.353			29.07.81	0.144		y
	23.07.82	0.235	y	y	25.07.82	0.205	y	y
0853+121	12.07.81	0.402	y	y	20.07.81	0.282	y	y
	22.07.81	0.252	y	y	25.07.81	0.207	y	y
0912+105	22.07.81	0.332	y		03.08.81	0.156		y
	27.07.82	0.261	y	y	31.07.82	0.201	y	y
0914+103	22.07.81	0.339			03.08.81	0.163		
	Nonscintillating							
0915+099	20.07.81	0.378		y	22.07.81	0.348	y	y
	25.07.81	0.303	y	y	29.07.81	0.244	y	y
	03.08.81	0.172		y				
0925+092	22.07.81	0.386	y	y	25.07.81	0.341	y	y
	29.07.81	0.281	y	y	03.08.81	0.207	y	y
	06.08.82	0.168		y	22.08.82	0.161		y

contd....

Table 5.5 contd...

1	2	3	4†	5†	6	7	8†	9†
0932+089	22.07.81	0.413	y	y	25.07.81	0.369		
	29.07.81	0.308	y		03.08.81	0.233	y	
1007+062	11.08.81	0.253	y	y	15.08.81	0.193	y	y
	18.08.81	0.150		y				
1033+038	18.08.81	0.254	y		26.08.81	0.137		
	22.08.82	0.197			Nonscintillating?			
1039+035	11.08.81	0.387			15.08.81	0.326		
	26.08.81	0.158			Nonscintillating			
1150-036	06.09.81	0.291			13.10.81	0.348	y	y
	12.09.82	0.201	y	y	09.10.82	0.280	y	y
	13.10.82	0.344	y	y	16.10.82	0.391		
1201-041	18.09.81	0.143		y	18.10.81	0.381	y	
	12.09.82	0.242	y	y	16.09.82	0.178		y
	15.10.82	0.329	y	y				
1220-059	22.09.81	0.160			18.10.81	0.300	y	
	21.10.81	0.348	y	y	23.10.81	0.380		
	19.09.82	0.212	y	y	25.09.82	0.119		y
1232-064	15.09.81	0.318			18.09.81	0.270	y	y
	22.09.81	0.205	y	y	25.09.81	0.157		y
	18.09.82	0.274	y	y	25.09.82	0.161		y
1244-079	15.09.81	0.372			29.09.81	0.148		
	25.09.82	0.216	y	y	26.09.82	0.200	y	y
1246-081	15.09.81	0.380	y	y	29.09.81	0.155		
	26.09.82	0.208	y	y	29.09.82	0.160		
1249-086	15.09.81	0.397			29.09.81	0.173		
	29.09.82	0.177		y	Nonscintillating?			
1256-092	30.09.81	0.185			03.10.81	0.137		
	30.09.82	0.189		y	Nonscintillating?			
1322-116	06.11.80	0.345			07.11.80	0.361	y	y
	22.09.81	0.423			25.09.81	0.376	y	y
	08.10.81	0.166		y	02.11.81	0.275	y	y
	07.11.81	0.357	y	y	09.10.82	0.154		y
1339-121.1	27.09.81	0.409	y	y	30.09.81	0.362	y	y
	04.10.81	0.297	y	y	09.10.81	0.215	y	y
	02.11.81	0.203	y	y	09.11.81	0.320	y	y
	16.10.82	0.102		y				
1343-124	10.11.80	0.323		y	27.09.81	0.426		
	30.09.81	0.379			05.10.81	0.299		y
	14.10.81	0.149		y	09.11.81	0.302		
	11.11.81	0.335	y	y	24.11.82	0.536		
	30.11.82	0.622	y	y				

contd...

Table 5.5 contd...

1	2	3	4†	5†	6	7	8†	9†
1344-127	10.11.80	0.320	y	y	05.10.81	0.303	y	y
	10.11.81	0.315	y	y	13.11.81	0.365	y	y
	17.10.82	0.108		y	06.11.82	0.244	y	y
	07.11.82	0.261	y	y	24.11.82	0.533	y	y
	30.11.82	0.619						
1348-129	06.11.80	0.237	y	y	07.11.80	0.254	y	y
	05.10.81	0.318	y	y	08.10.81	0.269	y	y
	10.11.81	0.299	y	y	20.11.81	0.461	y	y
	21.11.81	0.477	y	y	24.11.81	0.522	y	y
	27.11.81	0.567	y	y	29.11.81	0.596	y	y
	02.12.81	0.637	y	y	05.12.81	0.677	y	y
	07.12.81	0.703	y	y	12.12.81	0.763	y	y
	17.10.82	0.123		y	06.11.82	0.228	y	y
1416-156	16.11.80	0.283	y	y	23.11.80	0.398	y	y
	09.10.81	0.374	y	y	21.10.81	0.177		y
	23.10.81	0.143			30.11.82	0.500	y	y
	06.12.82	0.589						
1422-150	25.11.80	0.409	y		25.10.81	0.128		
	24.10.82	0.149		y				
1426-161	22.11.80	0.340			25.11.80	0.389		
	25.10.81	0.151			Nonscintillating			
1429-154	22.11.80	0.334	y	y	25.11.80	0.383		
	25.10.81	0.155						
1434-155	25.11.80	0.364	y	y	27.11.80	0.397	y	y
	25.10.81	0.175			28.10.81	0.123		
1445-161	16.11.80	0.165		y	22.11.80	0.268	y	y
	25.11.80	0.319	y	y	27.11.80	0.352	y	y
	25.10.81	0.222		y	30.10.81	0.136		y
1452-168	22.11.80	0.239	y	y	27.11.80	0.323		y
	30.10.81	0.166		y	20.11.81	0.200	y	y
	31.10.82	0.154		y	03.11.82	0.102		y
1456-165	23.10.80	0.295	y	y	24.10.80	0.279	y	y
	25.10.80	0.262	y	y	26.10.80	0.245	y	y
	31.10.80	0.160		y	22.11.80	0.224		y
	26.11.80	0.292	y	y	31.10.82	0.169		y
	06.12.82	0.448	y	y	15.12.82	0.584	y	y
1522-188	05.11.80	0.187		y	19.12.80	0.556	y	
	31.10.81	0.293	y	y	06.11.81	0.174		y
	28.11.81	0.211		y	01.12.81	0.262	y	y
	08.11.82	0.144		y	20.12.82	0.563	y	
1548-199	15.12.80	0.400	y	y	19.12.80	0.464		
	10.11.81	0.210			09.12.81	0.295	y	
	12.11.82	0.180		y				

contd....